

On Endmember Identification in Hyperspectral Images Without Pure Pixels: A Comparison of Algorithms

Javier Plaza · Eligius M.T. Hendrix ·
Inmaculada García · Gabriel Martín · Antonio Plaza

Published online: 25 March 2011
© Springer Science+Business Media, LLC 2011

Abstract Hyperspectral imaging is an active area of research in Earth and planetary observation. One of the most important techniques for analyzing hyperspectral images is spectral unmixing, in which mixed pixels (resulting from insufficient spatial resolution of the imaging sensor) are decomposed into a collection of spectrally pure constituent spectra, called *endmembers* weighted by their correspondent fractions, or *abundances*. Over the last years, several algorithms have been developed for automatic endmember extraction. Many of them assume that the images contain at least one pure spectral signature for each distinct material. However, this assumption is usually not valid due to spatial resolution, mixing phenomena, and other considerations. A recent trend in the hyperspectral imaging community is to design endmember identification algorithms which do not assume the presence of pure pixels. Despite the proliferation of this kind of algorithms, many of which are based on minimum enclosing simplex concepts, a rigorous quantita-

tive and comparative assessment is not yet available. In this paper, we provide a comparative analysis of endmember extraction algorithms without the pure pixel assumption. In our experiments we use synthetic hyperspectral data sets (constructed using fractals) and real hyperspectral scenes collected by NASA's Jet Propulsion Laboratory.

Keywords Hyperspectral imaging · Endmember extraction · Spectral unmixing · Minimum enclosing simplex

1 Introduction

Hyperspectral imaging has been transformed from a sparse research tool into a commodity product available to a broad user community [1]. The wealth of spectral information available from advanced hyperspectral imaging instruments currently in operation has opened new perspectives in many application domains, such as monitoring of environmental and urban processes or risk prevention and response, including—among others—tracking wildfires, detecting biological threats, and monitoring oil spills and other types of chemical contamination. Advanced hyperspectral instruments such as NASA's Airborne Visible Infra-Red Imaging Spectrometer (AVIRIS) [2] are now able to cover the wavelength region from 0.4 to 2.5 μm using more than 200 spectral channels, at nominal spectral resolution of 10 nm.

In hyperspectral imaging, endmember extraction is the process of selecting a collection of pure signature spectra of the materials present in a remotely sensed hyperspectral scene. These pure signatures are then used to decompose the scene into a set of so-called abundance fractions by means of a spectral unmixing algorithm. Most techniques available

J. Plaza (✉) · G. Martín · A. Plaza
Hyperspectral Computing Laboratory, Dept. Technology of
Computers and Communications, University of Extremadura,
Avda. de la Universidad s/n, 10071 Cáceres, Spain
e-mail: jplaza@unex.es

G. Martín
e-mail: gamahefpi@unex.es

A. Plaza
e-mail: aplaza@unex.es

E.M.T. Hendrix · I. García
Department of Computer Architecture, University of Málaga,
29071 Málaga, Spain

E.M.T. Hendrix
e-mail: Eligius.Hendrix@wur.nl

I. García
e-mail: igarcia@ual.es

in endmember extraction literature have been designed under the pure pixel assumption, i.e., they assume that the input hyperspectral data set contains at least one pure observation for each distinct material present in the collected scene, and therefore a search procedure aimed at finding the most spectrally pure signatures in the input scene is correct [3]. Techniques include, among many others [4], the orthogonal subspace projection (OSP) algorithm [5], the N-FINDR algorithm [6], a vertex component analysis (VCA) [7], the iterative error analysis (IEA) [8], and other approaches based on mathematical morphology [9] and lattice auto-associative memories [10, 11]. Maximum volume techniques, of which N-FINDR is a representative algorithm, have found wide acceptance in the community [12]. This technique looks for the set of pixels filling the largest possible volume by *inflating* a simplex inside the data.

Although the procedure adopted by N-FINDR has been quite successful when pure pixels are present in the original hyperspectral image, given the spatial resolution of state-of-the-art imaging spectrometers and the presence of the mixture phenomenon at different scales (even at microscopic levels), this assumption is not true for many nowadays images where pixels are completely mixed [13]. In order to deal with this important issue, other methods have been developed that do not assume the presence of pure signatures in the input data. Instead, these methods aim at generating *virtual* endmembers (not necessarily present in the set comprised by input data samples). Techniques in this category include volume minimization approaches inspired by the seminal minimum volume transform (MVT) algorithm [14], such as the minimum volume constrained non-negative matrix factorization method (MVC-NMF) [15], the minimum volume simplex analysis (MVSA) algorithm [16], the convex analysis-based minimum volume enclosing simplex algorithm (MVES) [17], the simplex identification via split augmented Lagrangian (SISAL) algorithm [18], or the iterative constrained endmembers (ICE) [19].

Despite the proliferation of endmember identification algorithms designed outside the pure pixel stream, available algorithms have not been rigorously compared by using a unified scheme. In this paper, we present a comparative study of endmember selection algorithms without the pure pixel assumption, using both simulated and real hyperspectral data sets. The major contributions of this work are: (1) the development of a framework and test set for experimental comparison of endmember selection algorithms without the pure pixel assumption, and (2) an assessment of the state of the art for endmember identification by drawing comparisons between substantially different approaches to the problem in rigorous fashion. The comparison includes algorithms with and without the pure pixel assumption, in a way that each method is fairly compared with others on the same common ground. The investigation in this paper follows the path initiated in [3], but substantially expands the

study by considering algorithms proposed in recent years and which present significant innovations with regards to methods designed under the pure pixel assumption. The latter category of algorithms may not be appropriate for analyzing data sets provided by the new generation of hyperspectral imaging instruments, which continue increasing their spectral resolution at the expense of maintaining (or even decreasing) the spatial resolution in the hope of imaging larger portions of the surface of the Earth.

The remainder of the paper is structured as follows. Section 2 describes the algorithms that will be compared in this study. Section 3 presents the comparative framework, performance criteria and test set, which comprises a database of simulated data sets (which have been generated in this work using fractals) and a real AVIRIS hyperspectral image. In Sect. 4, a comparative performance analysis for the algorithms described in Sect. 2 is presented and discussed. Finally, Sect. 5 points out main concluding statements derived from this paper and future research opportunities.

2 Endmember Identification Algorithms

In this section, we describe several endmember identification algorithms designed under the linear mixture model assumption. Let us denote the reflectance at channel i from a given pixel of the original hyperspectral image as follows:

$$y_i = \sum_{j=1}^p \rho_{ij} \alpha_j + w_i, \quad (1)$$

where ρ_{ij} denotes the reflectance of endmember j at wavelength λ_i , α_j denotes the abundance of endmember j at the considered pixel, and p is the number of endmembers. The abundances are generally subject to the abundance sum-to-one constraint (ASC) and the abundance non-negativity constraint (ANC):

$$\sum_{j=1}^p \alpha_j = 1, \quad \alpha_j \geq 0, \quad j = 1, \dots, p. \quad (2)$$

Let \mathbf{y}_i be an $B \times 1$ vector, where B is the total number of bands, and $\mathbf{m}_j \equiv [\rho_{1j}, \rho_{2j}, \dots, \rho_{Bj}]^T$ be the spectral signature of the j th endmember. Expression (1) can then be written in compact matrix form as:

$$\mathbf{Y} = \mathbf{M}\mathbf{S} + \mathbf{W}, \quad (3)$$

where \mathbf{Y} is a hyperspectral image made up of n pixel vectors in total, defined as $\mathbf{Y} \equiv [\mathbf{y}_1, \dots, \mathbf{y}_n] \in \mathbb{R}^{B \times n}$. $\mathbf{M} \equiv [\mathbf{m}_1, \mathbf{m}_2, \dots, \mathbf{m}_p] \in \mathbb{R}^{B \times p}$ is a matrix containing the signatures of the endmembers present in the pixel. $\mathbf{S} \equiv [\alpha_1, \dots, \alpha_n] \in \mathbb{R}^{p \times n}$ is a matrix containing the fractional abundances, and $\mathbf{W} \in \mathbb{R}^{B \times n}$ models additive noise. Several

techniques have been adopted in the literature to estimate the matrix of endmembers \mathbf{M} by assuming the presence or absence of pure pixels in the original hyperspectral data. In the following, we describe the most relevant approaches in each category.

2.1 Techniques Designed Under the Pure Pixel Assumption

These algorithms assume the presence in the original hyperspectral image of at least one pure pixel per endmember, meaning that there is at least one pixel containing \mathbf{m}_j for each endmember j being a vertex of the simplex encompassed by the data. Although this assumption enables the design of efficient algorithms from a computational point of view, it also imposes a requisite that may not hold in most real analysis scenarios.

One of the most widely used algorithms that include the pure pixel assumption is N-FINDR, which looks for the set of pixels with the largest possible volume by *inflating* a simplex inside the data. After a dimensionality reduction of the original hyperspectral image from B to $p - 1$, where the principal component analysis (PCA) [20] or the minimum noise fraction (MNF) [21] can be used for this purpose, the procedure begins with a random initial selection of pixels from the original image (see Fig. 1(a)), which results in an initial endmember matrix \mathbf{M} . Every pixel in the image is evaluated in order to refine the estimate of endmembers, looking for the set of pixels that maximizes the volume of the simplex defined by selected endmembers and calculated as follows:

$$V(\mathbf{M}) \equiv \frac{1}{(p-1)!} \left| \det \begin{bmatrix} 1 & 1 & \dots & 1 \\ \mathbf{m}_0 & \mathbf{m}_1 & \dots & \mathbf{m}_p \end{bmatrix} \right|. \quad (4)$$

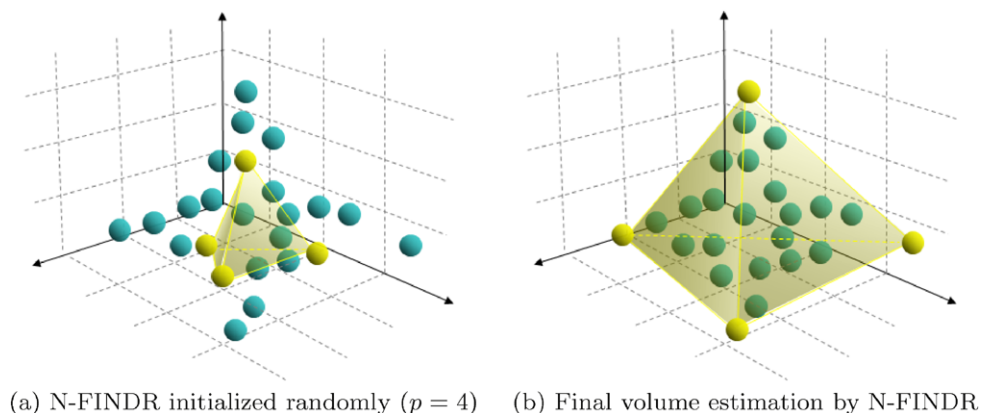
For every pixel the corresponding volume is checked if this pixel replaces one of the endmember positions in matrix \mathbf{M} . If the replacement results in an increase of volume, the pixel replaces the endmember. This procedure is repeated until there are no more endmember replacements (see Fig. 1(b)).

Another widely used approach is the OSP, which starts by selecting the pixel vector with maximum length in the scene as the first endmember. Then, it looks for the pixel vector with the maximum absolute projection in the space orthogonal to the space linearly spanned by the initial pixel, and labels that pixel as the second endmember. A third endmember is found by applying an orthogonal subspace projector [5] to the original image, where the signature that has the maximum orthogonal projection in the space orthogonal to the space linearly spanned by the first two endmembers. This procedure is repeated until the number of endmembers, p , has been reached [22].

The VCA algorithm also makes use of the concept of orthogonal subspace projections. However, as opposed to the OSP algorithm, VCA exploits the fact that the endmembers are the vertices of a simplex, and that the affine transformation of a simplex is also a simplex [7]. As a result, VCA uses a positive cone, which projected on an appropriately chosen hyperplane gives a simplex with vertices corresponding to the endmembers. After projecting the data onto the selected hyperplane, the VCA projects all image pixels to a random direction and uses the pixel with the largest projection as the first endmember. The other endmembers are identified in sequence by iteratively projecting the data onto a direction orthogonal to the subspace spanned by the endmembers already determined. The new endmember is then selected as the pixel corresponding to the extreme projection, and the procedure is repeated until a set of p endmembers is found.

Finally, the IEA algorithm implements a series of ASC and ANC-constrained unmixing operations, each time choosing as endmembers those pixels which minimize the remaining reconstruction error in the unmixed image. Optionally, each endmember can be averaged with the set of pixel vectors which are within a certain spectral angle value with regards to the extracted endmember. However, since spectral averaging generally decreases signature purity, in this work we have decided to use the IEA without spectral averaging hence the algorithm falls within this category. As a result, all the algorithms in the category that does not in-

Fig. 1 Graphical interpretation of the N-FINDR algorithm in a 3-dimensional space



clude the pure pixel assumption (described below) are based on minimum enclosing volume concepts.

2.2 Techniques Designed Without the Pure Pixel Assumption

Most of the techniques in this category adopt a minimum volume strategy aimed at finding the endmember matrix \mathbf{M} by minimizing the volume of the simplex defined by its columns and containing the endmembers. This is a non-convex optimization problem much harder than those considered in the previous subsection in which the endmembers are assumed to belong to the input hyperspectral image.

Craig's seminal work established the concepts regarding the algorithms of minimum volume type. The MVSA and SISAL algorithms implement a robust version of the minimum volume concept. The robustness is introduced by allowing the ANC to be violated. These violations are weighted using a soft constraint given by the hinge loss function ($\text{hinge}(x) = 0$ if $x \geq 0$ and $-x$ if $x < 0$). After reducing the dimensionality of the input data from B to $p - 1$, MVSA/SISAL aim at solving the following optimization problem:

$$\hat{\mathbf{Q}} = \arg \max_{\mathbf{Q}} \log(|\det(\mathbf{Q})|) - \lambda \mathbf{1}_p^T \text{hinge}(\mathbf{Q}\mathbf{Y})\mathbf{1}_n \quad (5)$$

$$\text{s.t.: } \mathbf{1}_p^T \mathbf{Q} = \mathbf{q}_m, \quad (6)$$

where $\mathbf{Q} \equiv \mathbf{M}^{-1}$, $\mathbf{1}_p$ and $\mathbf{1}_n$ are column vectors of ones of sizes p and n (n stands for the number of spectral vectors), respectively, $\mathbf{q}_m \equiv \mathbf{1}_p^T \mathbf{Y}_p^{-1}$ with \mathbf{Y}_p being any set of linearly independent spectral vectors taken from the hyperspectral data set \mathbf{Y} , and λ is a regularization parameter. Here, maximizing $\log(|\det(\mathbf{Q})|)$ is equivalent to minimizing $V(\mathbf{M})$.

The MVES algorithm aims at solving the optimization problem (5) with $\lambda = \infty$, i.e., for hard ANC but without using a de-noising strategy prior to the data analysis. Instead, MVES implements a cyclic minimization using linear programming. Although the optimization problem (5) is non-convex, it is proved in [17] that the existence of pure pixels is a sufficient condition for MVES to perfectly identify the true endmembers.

The MVC-NMF algorithm solves the following optimization problem applied to the original data set, i.e., without dimensionality reduction, as follows:

$$\hat{\mathbf{M}} = \arg \min_{\mathbf{M} \in \mathbb{R}^{B \times p}} \frac{1}{2} \|\mathbf{Y} - \mathbf{M}\mathbf{S}\|_F^2 + \lambda V^2(\mathbf{M}) \quad (7)$$

$$\text{s.t.: } \mathbf{M} \geq 0, \quad \mathbf{S} \geq 0, \quad \mathbf{1}^T \mathbf{S} = \mathbf{1}_n^T,$$

where $\|\mathbf{A}\|_F^2 \equiv \text{tr}(\mathbf{A}^T \mathbf{A})$ is the Frobenius norm of matrix \mathbf{A} and λ is a regularization parameter. The optimization (7) minimizes a two term objective function, where the term

$(1/2)\|\mathbf{Y} - \mathbf{M}\mathbf{S}\|_F^2$ measures the approximation error and the term $V^2(\mathbf{M})$ measures the square of the volume of the simplex defined by the columns of \mathbf{M} . The regularization parameter λ controls the tradeoff between the reconstruction errors and simplex volumes. MVC-NMF implements a sequence of alternate minimizations with respect to \mathbf{S} (quadratic programming problem) and with respect to \mathbf{M} (non-convex programming problem). The major difference between MVC-NMF and MVSA/SISAL algorithms is that the latter allows violations of the ANC, whereas the former does not.

Finally, we have recently developed a new minimum volume enclosing algorithm called MINVEST [23]. This algorithm adopts a hierarchical vision of the spectral unmixing problem. First, it uses PCA to reduce the dimensionality of the data from B to $p - 1$. Then, it minimizes the volume of an enclosing simplex in the reduced space while estimating the fractional abundance of vertices in simultaneous fashion. Although the concept of MINVEST is similar to that of other algorithms discussed in this section, a distinguishing feature is that MINVEST takes care of noise by iteratively identifying and removing pixels that fall outside the simplex to be estimated.

2.3 Illustrative Example Without Pure Pixels

To conclude this section, we illustrate via a simple toy example the potential advantages of algorithms without the pure pixel assumption. For this purpose, we have generated a toy data set made up of linear mixtures of three endmembers (designated as 'A', 'B' and 'C', respectively) where the maximum degree of purity of any of the considered endmembers in the available observations is given a maximum of 70% of an endmember. The endmembers have been randomly selected from a library of mineral spectral available online from U.S. Geological Survey (USGS). The simulated data set does not include any pure observations. A peculiarity of this situation is that, although the pure signatures 'A', 'B' and 'C' have been used to create all the simulated mixtures, the pure observations themselves (which can be considered as ground-truth) are not included in the input data to be processed. As a result, finding $p = 3$ endmembers in this toy example is a challenging problem. In this case, algorithms with the pure pixel assumption (e.g., N-FINDR) tackle the problem by finding the best combination that can be formed using samples contained in the data set. Quite opposite, minimum enclosing-based approaches (e.g., MINVEST) address the problem by finding the simplex with minimum volume that can enclose all the observations. The situation is graphically illustrated in Fig. 2, which plots the outcome of the endmember identification process by N-FINDR and MINVEST in a two-dimensional space given by the first two PCA components. As shown in Fig. 2, only MINVEST can

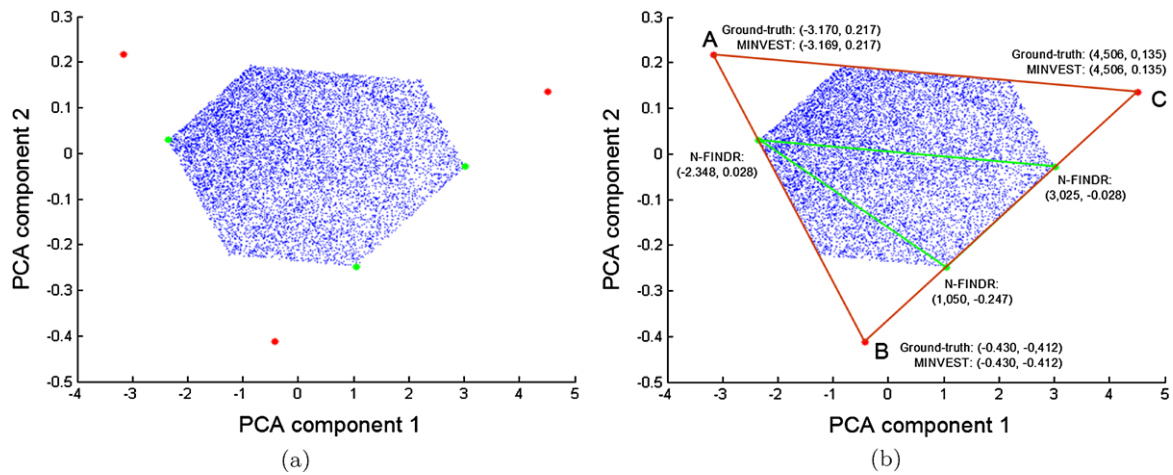


Fig. 2 (Color online) (a) Two-dimensional representation of a toy data set without pure samples, and endmembers extracted by MINVEST (red) and N-FINDR (green). (b) Coordinates of the endmembers and simplices defined by the endmembers extracted by MINVEST (red) and N-FINDR (green)

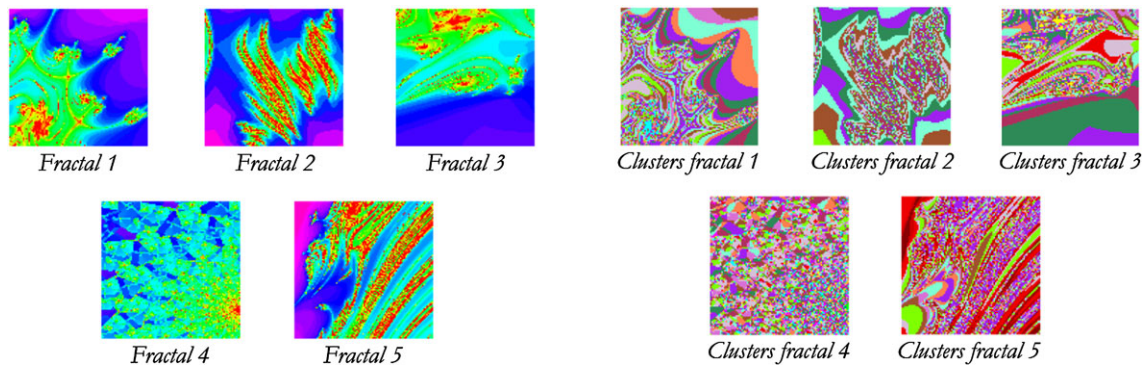


Fig. 3 Synthetic images, where spatial patterns were generated using fractals (left) then segmented into clusters (right)

successfully retrieve the endmembers (even if these are not contained in the input data).

3 Framework, Test Set and Criteria

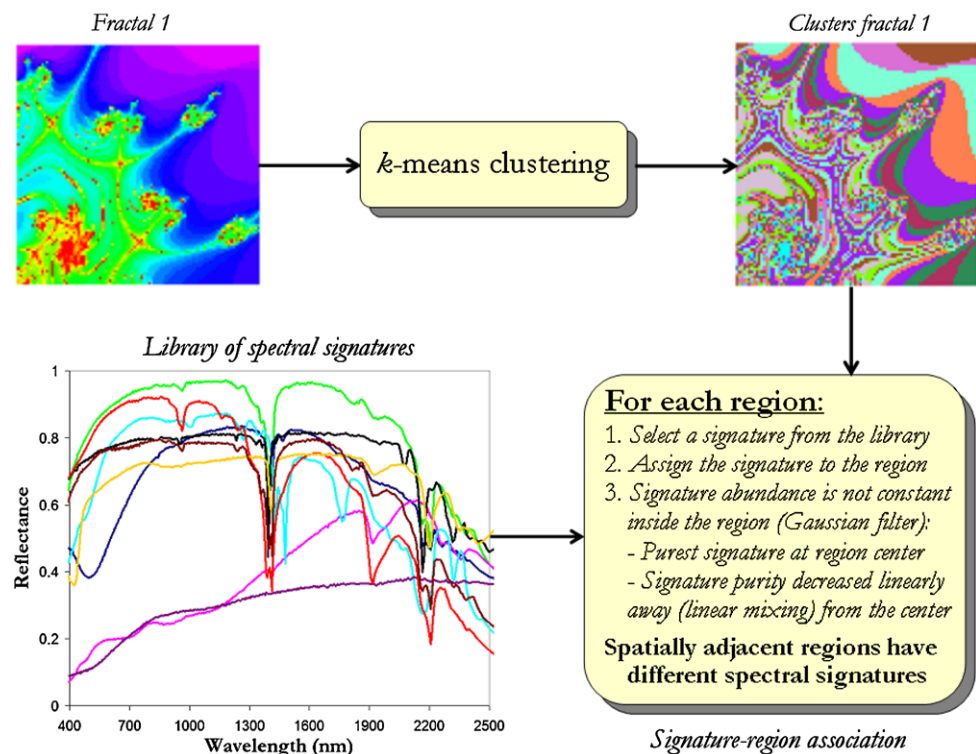
3.1 Synthetic Hyperspectral Data

A database of five 100×100 -pixel synthetic hyperspectral scenes has been created using fractals to generate distinct spatial patterns, which are then used to simulate linear mixtures of a set of endmember signatures randomly selected from a spectral library compiled by the U.S. Geological Survey (USGS)¹ and made up of a total of 420 spectral signatures. The leftmost part of Fig. 3 displays the five fractal images used in the simulations. These images are further divided into a number of clusters using the k -means algorithm in [24], where the number of clusters extracted from

the five fractal images was always larger than the number of endmember signatures, fixed in our experiments to $p = 9$. The resulting clusters are displayed in the rightmost part of Fig. 3. A crucial step in the simulation procedure is how to assign a spectral signature to each cluster. For this purpose, we have implemented an automatic procedure that follows a simple strategy in which the $p = 9$ signatures are first assigned to spatially disjoint regions belonging to different clusters. The remaining regions are then assigned spectral signatures in an automatic way, ensuring that: (1) spatially adjacent clusters always have different signatures associated to them, and (2) there is a balance among the overall number of pixels in the image which are associated to each spectral signature. Inside each region, the abundance proportions of spectral signatures have been generated following a procedure that tries to imitate reality as much as possible, i.e. those pixels closer to the borders of the regions are more heavily mixed, while the pixels located at the center of the regions are more spectrally pure in nature. This is accomplished by linearly mixing the signature associated to each cluster with those associated to neighboring clusters, mak-

¹<http://speclab.cr.usgs.gov/spectral-lib.html>.

Fig. 4 Block diagram describing our procedure for generating synthetic hyperspectral images



ing sure that the most spectrally pure signature remains at the center of the region while signature purity decreases linearly away from the center to the borders of the regions. For this purpose, a Gaussian filter is applied where the width of the Gaussian is carefully adjusted according to the width of each window. With the aforementioned procedure, which is graphically illustrated by a block diagram in Fig. 4, the simulated regions exhibit the following properties:

1. All the simulated pixels inside a region are mixed, and the simulated image does not contain completely pure pixels. This increases the complexity of the unmixing problem and simulates the situation often encountered in real-world analysis scenarios, in which completely pure pixels are rarely found.
2. Pixels close to the borders of the region are more heavily mixed than those in the center of the region.
3. If the simulated region is sufficiently large, the pixels located at the center can exhibit a degree of purity of 99% of a certain endmember. However, if the size of the simulated region is small, the degree of purity of pixels at the center of the region can decrease until 95% of a certain endmember, while pixels located in the region borders are generally more heavily mixed.

To conclude the simulation process, zero-mean Gaussian noise was added to the scenes in different signal to noise ratios (SNRs)—from 30 to 110—to simulate contributions from ambient and instrumental sources, following the procedure described in [5]. For illustrative purposes, Fig. 5 shows

the spectra of the USGS signatures used in the simulation of one of the synthetic scenes (the one labeled as “Fractal 1” in Fig. 3). The full database of simulated hyperspectral images is available online.² The abundance maps associated to each reference USGS signature in the construction of the synthetic scene are also displayed in Fig. 5, where black color indicates 0% abundance of the corresponding mineral, white color indicates 100% abundance of the mineral, and the fractional abundances in each pixel of the scene sum to unity, thus ensuring that the simulated fractal images strictly adhere to a fully constrained linear mixture model.

Finally, we emphasize that other methods exist for performance evaluation of endmember extraction and hyperspectral imaging algorithms using synthetic hyperspectral images. Of particular relevance is a Matlab toolbox (available online³) for generating synthetic endmember abundances using random fields and Legendre polynomials [25].

3.2 Real Hyperspectral Data

The real hyperspectral data set used in our experiments is the well-known AVIRIS Cuprite data set, available online in reflectance units⁴ after atmospheric correction. This scene has

²<http://www.umbc.edu/rssipl/people/aplaza/fractals.zip>.

³http://www.ehu.es/ccwintco/index.php/Hyperspectral_Imagery_Synthesis_tools_for_MATLAB.

⁴<http://aviris.jpl.nasa.gov/html/aviris.freedata.html>.

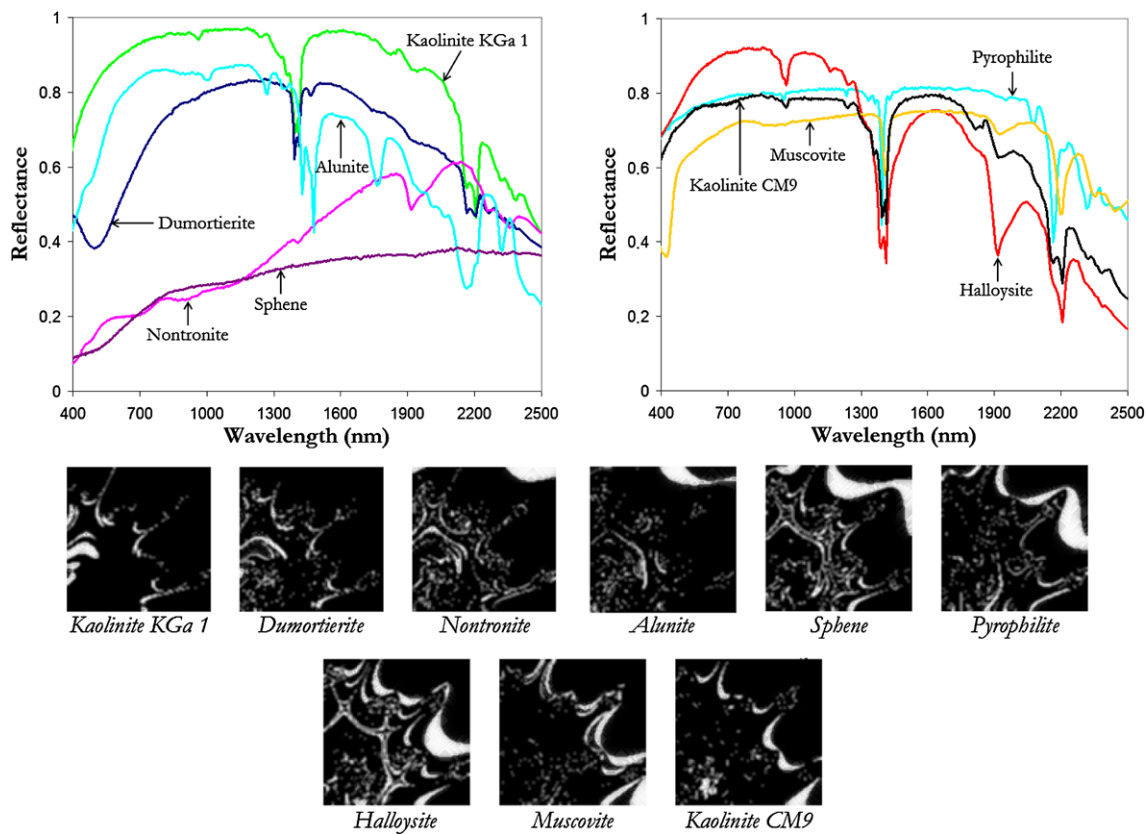


Fig. 5 USGS library signatures (*top*) and fractional abundance distributions (*bottom*) considered for generating the simulated hyperspectral scene labeled as “Fractal 1” in experiments

been widely used to validate the performance of endmember extraction algorithms. The portion used in our experiments corresponds to a 150×150 -pixel subset of the image sector labeled as f970619t01p02_r02_sc03.a.rfi in the online data, which were collected in 1997. The scene comprises 224 spectral bands between 0.4 and 2.5 μm , with full width at half maximum of 10 nm and spatial resolution of 20 meters per pixel. Prior to the analysis, several bands were removed due to water absorption and low SNR in those bands, leaving a total of 192 reflectance channels to be used in the experiments. The Cuprite site is well understood mineralogically [26], and has several exposed minerals of interest included in a spectral library compiled by the U.S. Geological Survey (USGS).⁵

3.3 Performance Criteria

We describe two criteria that can be used in the comparison of the performance of endmember extraction and spectral unmixing algorithms in the synthetic fractal and real scenes. The first metric is the spectral angle (SA) [27] between each extracted endmember and the available USGS ground-truth

spectral signatures. This metric is equivalent to the absolute value of correlation. Low SA scores mean high spectral similarity between the compared vectors (the value range of SA is $[0, 90]$ degrees). This spectral similarity measure is invariant under the multiplication of pixel vectors by constants and, consequently, is invariant to unknown multiplicative scalings that may arise due to differences in illumination and angular orientation. The SA allows us to identify the USGS signature which is most similar to each endmember by observing the minimum SA distance reported for such endmember across the entire set of available USGS signatures using the following spectral similarity matching algorithm. Let us denote by $\mathbf{M} \equiv [\mathbf{m}_1, \mathbf{m}_2, \dots, \mathbf{m}_p]$ the set of p endmembers extracted by a certain algorithm from a hyperspectral scene, and let $\mathbf{G} \equiv [\mathbf{g}_1, \mathbf{g}_2, \dots, \mathbf{g}_q]$ denote a set of ground-truth spectral signatures. Note that the number of extracted endmembers, p , might be different from the number of available ground-truth signatures, q . With this in mind, we can establish the correspondence between ground-truth endmembers in set \mathbf{G} and the endmembers obtained from the image data in set \mathbf{M} as follows:

1. *Initialization.* Label all endmembers in sets \mathbf{G} and \mathbf{M} as ‘unmatched.’

⁵<http://speclab.cr.usgs.gov/spectral-lib.html>.

Table 1 Average spectral similarity scores (in degrees) between the USGS mineral spectra and their corresponding endmember pixels produced by several endmember extraction algorithms across the five synthetic scenes in Fig. 3

Algorithm	SNR = 30	SNR = 50	SNR = 70	SNR = 90	SNR = 110	SNR = ∞
IEA	2.087	0.460	0.349	0.342	0.342	0.342
N-FINDR	2.089	0.464	0.384	0.389	0.362	0.362
OSP	2.118	0.452	0.350	0.361	0.345	0.365
VCA	2.188	0.520	0.368	0.434	0.436	0.400
MINVEST	7.477	1.221	0.228	0.149	0.164	0.162
MVC-NMF	1.558	0.384	0.383	0.351	0.374	0.316
MVES	12.569	1.436	0.279	0.085	0.042	0.108
MVSA	15.256	1.365	0.130	0.028	0.024	0.024
SISAL	12.754	1.256	0.206	0.142	0.212	0.154

2. *Matching.* For each unmatched endmember in set \mathbf{G} , calculate the SA between such endmember and all endmembers in the set \mathbf{M} . If a certain pair $\{\mathbf{m}_i, \mathbf{g}_j\}$, with $1 \leq i \leq p$ and $1 \leq j \leq q$, results in the minimum obtained value of $\text{SA}(\mathbf{m}_i, \mathbf{g}_j)$ after comparing all possible combinations of endmembers across the two sets, then label the associated endmembers, \mathbf{m}_i and \mathbf{g}_j as ‘matched.’
3. *Iterative procedure and termination.* Each time a pair of endmembers $\{\mathbf{m}_i, \mathbf{g}_j\}$ has been ‘matched’, the endmember \mathbf{m}_i is removed from the set \mathbf{M} and the endmember \mathbf{g}_j is removed from the set \mathbf{G} . Once these endmembers have been removed, the process is repeated from step 2 until all endmembers in set \mathbf{G} have been labeled as ‘matched.’

A second criterion to measure the goodness of the reconstruction is the root mean square error (RMSE) between the original and the reconstructed hyperspectral scene. Let us assume that \mathbf{Y} is the original hyperspectral image, and that $\hat{\mathbf{Y}}$ is a reconstructed version of \mathbf{Y} , obtained using (3) with a set of endmembers \mathbf{M} , automatically derived by a certain algorithm from the original scene, and their corresponding fractional abundances. Let us also assume that the pixel vector \mathbf{y}_j in the original image is given by $\mathbf{y}_j \equiv [y_{1j}, y_{2j}, \dots, y_{Bj}]$, while the corresponding pixel vector in the reconstructed hyperspectral scene is given by $\hat{\mathbf{y}}_j \equiv [\hat{y}_{1j}, \hat{y}_{2j}, \dots, \hat{y}_{Bj}]$, with $j = 1, \dots, p$. With the above notation in mind, the RMSE between the original and the reconstructed hyperspectral scenes can be calculated as follows:

$$\text{RMSE}(\mathbf{Y}, \hat{\mathbf{Y}}) = \frac{1}{p} \sum_{i=1}^p \left(\frac{1}{B} \sum_{j=1}^B [y_{ji} - \hat{y}_{ji}]^2 \right)^{\frac{1}{2}}. \quad (8)$$

It should be noted that the RMSE metric is based on the assumption that a set of high-quality endmembers may allow reconstruction of the original hyperspectral scene with higher precision than a set of low-quality endmembers, regardless of the presence of such endmembers in the original scene or not.

4 Comparison of Algorithms

The exact algorithms to be compared are described first in Sect. 4.1. This is followed by the performance comparison on the synthetic data in Sect. 4.2 and on the real data (Sect. 4.3).

4.1 Algorithms Used in Our Comparison

The algorithms selected for demonstration purposes comprise four endmember extraction algorithms which assume the presence of pure pixels in the scene (IEA, N-FINDR, OSP and VCA) and five endmember identification algorithms which do not assume the presence of pure pixels in the input scene (MINVEST, MVC-NMF, MVES, MVSA and SISAL). The Matlab codes of MVC-NMF, MVES, MVSA, SISAL and VCA have been obtained from the algorithm developers, while the other algorithms have been carefully implemented by us according to the original descriptions available in the literature and with the recommended parameter settings in each case. Specifically, our Matlab implementations of N-FINDR, OSP and IEA algorithms are available online.⁶ The Matlab implementations of MINVEST,⁷ MVSA,⁸ SISAL,⁹ and VCA¹⁰ are also available.

4.2 Experiments with Synthetic Data

Table 1 shows the average spectral similarity scores (in degrees) between the reference USGS mineral spectra and their corresponding endmember pixels produced by several

⁶<http://www.umbc.edu/rssi/pl/people/aplaza/codes.zip>.

⁷<http://www.umbc.edu/rssi/pl/people/aplaza/minvest.zip>.

⁸http://www.lx.it.pt/~bioucas/code/mvsa_demo.zip.

⁹http://www.lx.it.pt/~bioucas/code/sisal_demo.zip.

¹⁰http://www.lx.it.pt/~bioucas/code/demo_vca.zip.

Table 2 Average RMSE scores after reconstructing the five synthetic scenes in Fig. 3 using the extracted endmembers

Algorithm	SNR = 30	SNR = 50	SNR = 70	SNR = 90	SNR = 110	SNR = ∞
IEA	0.3566	0.0398	0.0107	0.0088	0.0087	0.0087
N-FINDR	0.3563	0.0392	0.0095	0.0075	0.0080	0.0080
OSP	0.3590	0.0394	0.0100	0.0083	0.0088	0.0091
VCA	0.3692	0.0446	0.0171	0.0217	0.0187	0.0106
MINVEST	0.2982	0.0364	0.0041	0.0009	0.0008	0.0008
MVC-NMF	0.3268	0.0345	0.0190	0.0124	0.0135	0.0125
MVES	0.2968	0.0296	0.0029	0.0005	0.0004	0.0004
MVSA	0.2963	0.0296	0.0030	0.0005	0.0004	0.0004
SISAL	0.2969	0.0297	0.0023	0.0005	0.0004	0.0004

endmember identification algorithms, across the five synthetic scenes in Fig. 3. As a result, each value reported in Table 1 corresponds to the average SA obtained after processing the five considered scenes with the same SNR (five different SNR values, ranging from 30 to 110, together with the no-noise scenario are reported in the table). In all cases, the number of endmembers to be detected was set to $p = 9$ which is the number of different spectral signatures used to simulate each scene.

Table 1 reveals that, as expected, under extremely high noise conditions ($\text{SNR} \leq 30$) the algorithms which assume the presence of pure pixels in the original image outperform those without the pure pixel assumption. This is because extreme noise can significantly affect the construction of the minimum enclosing simplex, thus resulting in endmembers which are far away from the actual pixel observations. In this particular scenario, the MVC-NMF provides a better characterization of noise by violating the ANC, which allows for the identification of endmembers which are closer to the actual observations. For $\text{SNR} = 50$ all algorithms provide very similar spectral angle values with regards to the USGS reference spectra, i.e. within a range below 1.5° in all cases. As the SNR is increased (e.g. $\text{SNR} \geq 70$) the algorithms without the pure pixel assumption generally outperform the algorithms with the pure pixel assumption, with both MVSA and SISAL providing the best spectral angle similarity scores across all methods.

On the other hand, Table 2 displays the average RMSE scores after reconstructing the five synthetic scenes in Fig. 3 using the endmembers extracted by several methods. The table shows that, in most cases, the algorithms which do not assume the existence of pure pixels outperform those assuming the presence of pure pixels in the hyperspectral image. For high noise condition ($\text{SNR} \leq 30$) the performance of all algorithms is similar. However, even in this scenario the algorithms without the pure pixel assumption tend to perform slightly better than the algorithms with the pure pixel assumption. As the SNR increases, algorithms

such as MVSA and SISAL (and also MVES) generally provide the best performance among the algorithms without the pure pixel assumption, while MVC-NMF provides slightly higher reconstruction errors. This is probably due to the fact that MVC-NMF has less flexibility with constraints than MVSA/SISAL have.

To conclude this subsection, we emphasize that the SNR values observed in real hyperspectral imaging instruments are ever-increasing, and hence the consideration of low SNR values in our experiments should not be considered as indicative of real parameter values in state of the art hyperspectral imaging instruments. Instead, we are testing our algorithms under high noise conditions in order to evaluate their sensitivity to this parameter. For instance, the SNR in the AVIRIS sensor at the time of the acquisition of the real hyperspectral image over the Cuprite mining district in Nevada in 1997 was considerably higher than the values used in computer simulations: the highest SNR levels calculated for a 50% reflectance target was measured in the wavelength at $0.7 \mu\text{m}$ to levels of $\text{SNR} = 1000$, while the lowest was measured in the wavelength at $2.2 \mu\text{m}$ with levels of $\text{SNR} = 400$. In the following section, we conduct an experiment with this real hyperspectral image.

4.3 Experiments with Real Data

In this subsection we report the RMSE scores after reconstructing the AVIRIS Cuprite image using the endmembers extracted by several methods. Due to the fact that the USGS library spectra are acquired under different conditions as the airborne data, we have decided to avoid SA-based comparisons in this subsection. This is because we consider that the evaluation of the performance of the different algorithms would be directly related with the quality of the atmospheric correction algorithm applied to convert the at-sensor radiance data into reflectance units. We did not have any control on such algorithm since we directly used the reflectance data available in AVIRIS website. Hence, we focus only on the

use of the RMSE metric. In all our experiments, the number of endmembers to be identified was set to $p = 9$ after the consensus reached between two of the most popular methods for estimating the number of endmembers in hyperspectral data: HySime [28] and the VD concept [29], implemented using $P_F = 10^{-3}$ as the input false alarm probability.

As shown in Table 3, the tendency of the results is similar to that of the experiments with synthetic scenes for moderately high SNR values; the algorithms which assume the presence of pure pixels in the image provide significantly higher reconstruction errors than those without the pure pixel assumption. For illustrative purposes, Fig. 6 shows the error maps obtained after reconstructing the AVIRIS Cuprite scene using $p = 9$ endmembers identified by different methods. As shown by Fig. 6, the algorithms with the pure pixel assumption produce higher overall and specific reconstruction errors in certain areas (this is related to incorrectly se-

lected or missing endmembers for these areas). However, the algorithms without the pure pixel assumption clearly avoid these modeling errors at the reconstruction level, although further studies should be conducted in order to analyze the physical interpretation of the endmembers derived using such algorithms.

5 Conclusions and Future Research

Many endmember identification algorithms have been proposed in the literature over the past decade in the context of hyperspectral image analysis. Comparing these approaches has been a challenging task due to a lack of rigorous criteria to substantiate any new algorithm. This paper provides a framework to evaluate algorithms consisting of a test set of both simulated and real hyperspectral images and performance criteria. Algorithms of two categories, based on and not based on the pure pixel assumption are compared within this framework. A comparison of methods has been carried out from two different scopes. First, the issue was undertaken under the assumption that reliable ground-truth spectral signatures are available via synthetic hyperspectral images. A further experiment was conducted using real AVIRIS hyperspectral data and an image reconstruction-based criterion. In both cases, we have observed that algorithms without the pure pixel assumption generally outperform those methods in the other considered category, although there is still an issue related with the quality of the generated endmembers from the viewpoint of spectral signature quality (particularly when the hyperspectral data is acquired under high noise conditions). However, given the fact that the signal to noise ratios observed in hyperspec-

Table 3 Average RMSE scores after reconstructing the AVIRIS Cuprite image using the extracted endmembers

Algorithm	Average RMSE
IEA	0.1599
N-FINDR	0.1068
OSP	0.4184
VCA	0.1007
MINVEST	0.0393
MVC-NMF	0.0403
MVES	0.0392
MVSA	0.0392
SISAL	0.0393

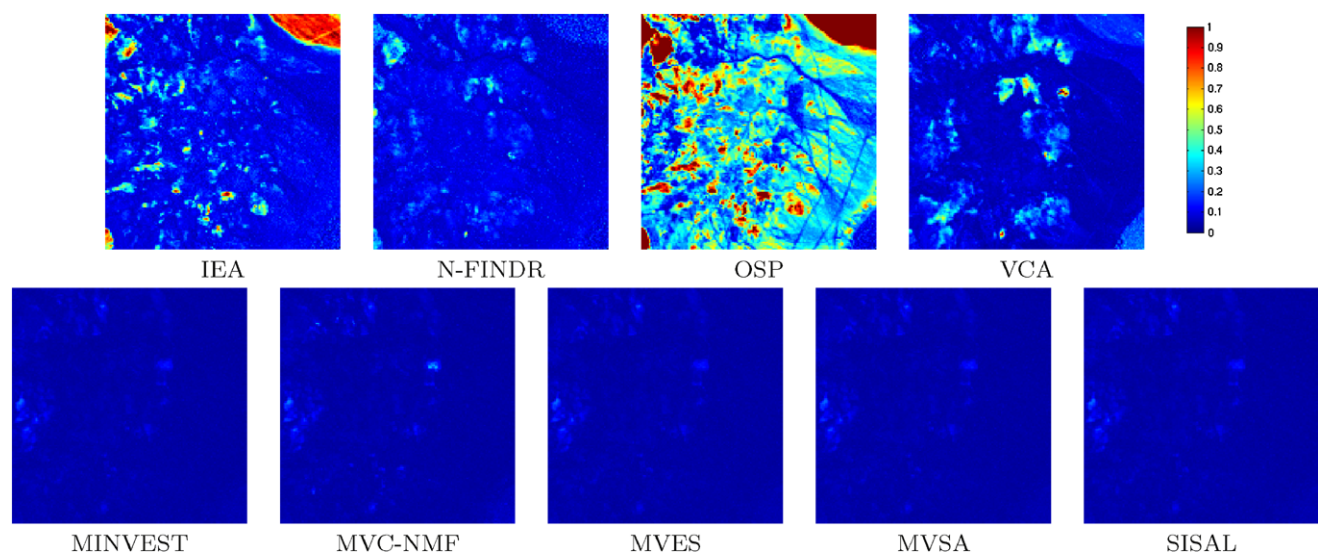


Fig. 6 Errors measured for various endmember identification algorithms after reconstructing the AVIRIS Cuprite scene

tral imaging instruments are ever-increasing, our comparative study confirms that the recent change of trend in the design of endmember identification algorithms may well be associated to the superior quality of these algorithms under moderate to low noise conditions.

Despite our effort to conduct a comprehensive, impartial, and rigorous comparative analysis of various algorithms, completion is not claimed. The designed framework leaves space for further comparison of algorithms. The number of algorithms based on the pure pixel assumption compared in this work is four, while five methods are compared in the category of algorithms without the pure pixel assumption. All methods included in our study have been selected based on their availability and on the fact that they represent very different design alternatives. In contrast, the application of the proposed comparative framework to a larger number of real images with high-quality ground-truth data is required in order to extrapolate the main conclusions drawn from the present study. Although the spectral quality of the endmembers produced by the methods without the pure pixel assumption has been shown to be appropriate in the synthetic data experiments, further studies related to the physical meaning of the endmembers derived by such methods from real hyperspectral data sets should be conducted.

Acknowledgements This work has been funded by grants from the Spanish Ministry of Science and Innovation (AYA2008-05965-C04-02, TIN2008-01117 and TIN2007-29664-E), Junta de Andalucía (P08-TIC-3518), in part financed by the European Regional Development Fund (ERDF) and the Marie Curie RTN (MRTN-CT-2006-035927). We gratefully thank the developers of the MVSA, SISAL and VCA algorithms for making their Matlab implementations publicly available, and the authors of MVES and MVC-NMF algorithms for sharing their Matlab implementations with us. Last but not least, we thank the anonymous reviewers for their outstanding comments and suggestions for improving the technical content and presentation of our manuscript.

References

- Goetz, A.F.H., Vane, G., Solomon, J.E., Rock, B.N.: Imaging spectrometry for Earth remote sensing. *Science* **228**, 1147–1153 (1985)
- Green, R.O., Eastwood, M.L., Sarture, C.M., Chrien, T.G., Aronsson, M., Chippendale, B.J., Faust, J.A., Pavri, B.E., Chovit, C.J., Solis, M., et al.: Imaging spectroscopy and the airborne visible/infrared imaging spectrometer (AVIRIS). *Remote Sens. Environ.* **65**(3), 227–248 (1998)
- Plaza, A., Martinez, P., Perez, R., Plaza, J.: A quantitative and comparative analysis of endmember extraction algorithms from hyperspectral data. *IEEE Trans. Geosci. Remote Sens.* **42**(3), 650–663 (2004)
- Du, Q., Raksuntorn, N., Younan, N.H., King, R.L.: End-member extraction for hyperspectral image analysis. *Appl. Opt.* **47**, 77–84 (2008)
- Harsanyi, J.C., Chang, C.-I.: Hyperspectral image classification and dimensionality reduction: An orthogonal subspace projection. *IEEE Trans. Geosci. Remote Sens.* **32**(4), 779–785 (1994)
- Winter, M.E.: N-FINDR: an algorithm for fast autonomous spectral end-member determination in hyperspectral data. In: *Proc. SPIE Image Spectrometry V*, vol. 3753, pp. 266–277 (2003)
- Nascimento, J.M.P., Bioucas-Dias, J.M.: Vertex component analysis: A fast algorithm to unmix hyperspectral data. *IEEE Trans. Geosci. Remote Sens.* **43**(4), 898–910 (2005)
- Neville, R.A., Staenz, K., Szeredi, T., Lefebvre, J., Hauff, P.: Automatic endmember extraction from hyperspectral data for mineral exploration. In: *Proc. 21st Canadian Symp. Remote Sens.*, pp. 21–24 (1999)
- Plaza, A., Martinez, P., Perez, R., Plaza, J.: Spatial/spectral endmember extraction by multidimensional morphological operations. *IEEE Trans. Geosci. Remote Sens.* **40**(9), 2025–2041 (2002)
- Grana, M., Villaverde, I., Maldonado, J., Hernandez, C.: Two lattice computing approaches for the unsupervised segmentation of hyperspectral images. *Neurocomputing* **72**, 2111–2120 (2009)
- Ritter, G.X., Urcid, G.: A lattice matrix method for hyperspectral image unmixing. *Inf. Sci.* **181**(10), 1787–1803 (2011)
- Zortea, M., Plaza, A.: A quantitative and comparative analysis of different implementations of N-FINDR: A fast endmember extraction algorithm. *IEEE Geosci. Remote Sens. Lett.* **6**, 787–791 (2009)
- Plaza, J., Plaza, A., Perez, R., Martinez, P.: On the use of small training sets for neural network-based characterization of mixed pixels in remotely sensed hyperspectral images. *Pattern Recognit.* **42**, 3032–3045 (2009)
- Craig, M.D.: Minimum-volume transforms for remotely sensed data. *IEEE Trans. Geosci. Remote Sens.* **32**, 542–552 (1994)
- Miao, L., Qi, H.: Endmember extraction from highly mixed data using minimum volume constrained nonnegative matrix factorization. *IEEE Trans. Geosci. Remote Sens.* **45**, 765–777 (2007)
- Li, J., Bioucas-Dias, J.: Minimum volume simplex analysis: a fast algorithm to unmix hyperspectral data. In: *Proc. IEEE International Geoscience and Remote Sensing Symposium*, vol. 3, pp. 250–253 (2008)
- Chan, T.-H., Chi, C.-Y., Huang, Y.-M., Ma, W.-K.: A convex analysis-based minimum-volume enclosing simplex algorithm for hyperspectral unmixing. *IEEE Trans. Signal Process.* **57**, 4418–4432 (2009)
- Bioucas-Dias, J.: A variable splitting augmented Lagrangian approach to linear spectral unmixing. In: *First IEEE GRSS Workshop on Hyperspectral Image and Signal Processing- WHISPERS'2009* (2009)
- Berman, M., Kiiveri, H., Lagerstrom, R., Ernst, A., Dunne, R., Huntington, J.F.: ICE: a statistical approach to identifying endmembers in hyperspectral images. *IEEE Trans. Geosci. Remote Sens.* **42**(10), 2085–2095 (2004)
- Richards, J.A., Jia, X.: *Remote Sensing Digital Image Analysis: An Introduction*. Springer, Berlin (2006)
- Green, A.A., Berman, M., Switzer, P., Craig, M.D.: A transformation for ordering multispectral data in terms of image quality with implications for noise removal. *IEEE Trans. Geosci. Remote Sens.* **26**, 65–74 (1988)
- Ren, H., Chang, C.-I.: Automatic spectral target recognition in hyperspectral imagery. *IEEE Trans. Aerosp. Electron. Syst.* **39**(4), 1232–1249 (2003)
- Hendrix, E.M.T., Garcia, I., Plaza, J., Plaza, A.: Minimum volume simplicial enclosure for spectral unmixing. Working Paper Mansholt Graduate School MPW-50, Wageningen University (2010). <http://www.wass.wur.nl/NR/rdonlyres/7270E45E-AB79-4DD5-8E2A-29556BE14A98/101189/201050def.pdf>
- Hartigan, J.A., Wong, M.A.: Algorithm as 136: A *k*-means clustering algorithm. *J. R. Stat. Soc., Ser. C, Appl. Stat.* **28**, 100–108 (1979)

25. Veganzones, M.A., Hernandez, C.: On the use of a hybrid approach to contrast endmember induction algorithms. In: Lecture Notes in Artificial Intelligence, vol. 6077, pp. 69–76 (2010)
26. Clark, R.N., Swayze, G.A., Livo, K.E., Kokaly, R.F., Sutley, S.J., Dalton, J.B., McDougal, R.R., Gent, C.A.: Imaging spectroscopy: Earth and planetary remote sensing with the usgs tetracorder and expert systems. *J. Geophys. Res.* **108**, 1–44 (2003)
27. Keshava, N., Mustard, J.F.: Spectral unmixing. *IEEE Signal Process. Mag.* **19**(1), 44–57 (2002)
28. Bioucas-Dias, J.M., Nascimento, J.M.P.: Hyperspectral subspace identification. *IEEE Trans. Geosci. Remote Sens.* **46**(8), 2435–2445 (2008)
29. Chang, C.-I., Du, Q.: Estimation of number of spectrally distinct signal sources in hyperspectral imagery. *IEEE Trans. Geosci. Remote Sens.* **42**(3), 608–619 (2004)



Javier Plaza received the M.S. and Ph.D. degrees in computer engineering from the University of Extremadura, Caceres, Spain in 1999 and 2002, respectively. He is currently an Assistant Professor with the Department of Technology of Computers and Communications of the University of Extremadura, and a member of the Hyperspectral Computing Laboratory. He has been a Visiting Researcher with the Remote Sensing Signal and Image Processing Laboratory, University of Maryland Baltimore County,

Baltimore; and with the AVIRIS Data Facility, Jet Propulsion Laboratory, Pasadena, CA. He is the author or coauthor of more than 100 publications on remotely sensed hyperspectral imaging, including more than 20 Journal Citation Report papers, book chapters, and conference proceeding papers. His research interests include remotely sensed hyperspectral imaging, pattern recognition, signal and image processing, and efficient implementation of large-scale scientific problems on parallel and distributed computer architectures.

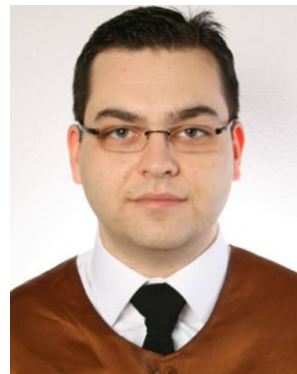


Eligius M.T. Hendrix obtained his Bachelor and Master degree in Econometrics from Tilburg University in 1984 and 1987 respectively. He was assistant professor Operations Research at the mathematics and social science department of Wageningen University up to 2005, where he also obtained his Ph.D. degree in 1998. After that he was associate professor Operations Research at Wageningen University and obtained a Ramon y Cajal researcher position in 2008 at the department of Computer Architecture at Málaga

University, where he is now. Research interests are in Global Optimization algorithms and its applications. He is editor of the *Journal of Global Optimization* and co-authored several books and articles in this area.



Inmaculada García received a B.Sc. degree in physics in 1977 from the Complutense University of Madrid, Spain, and a Ph.D. degree in 1986 from the University of Santiago de Compostela, Spain. From 1977 to 1987, she was an assistant professor, associate professor during 1987–1997, between 1997 and 2010 full professor at the University of Almeria and since 2010 full professor at the University of Malaga. She was head of the Department of Computer Architecture and Electronics at the University of Almeria for more than 12 years. During 1994–1995 she was a visiting researcher at the University of Pennsylvania, Philadelphia. She is head of the supercomputing-algorithms research group. Her research interest lies in the field of parallel algorithms for irregular problems related to image processing, global optimization, and matrix computation.



Gabriel Martín received the Computer Engineer degree from the University of Extremadura in 2008, and the Ms.C. degree from the same University in 2010. He is currently a Pre-Doctoral Research Associate with the Hyperspectral Computing Laboratory. His research interests comprise the development of new techniques for unmixing remotely sensed hyperspectral data sets as well as the efficient processing and interpretation of these data in different types of high performance computing architectures.



Antonio Plaza received the M.S. and Ph.D. degrees in computer engineering from the University of Extremadura, Caceres, Spain in 1999 and 2002, respectively. He was a Visiting Researcher with the Remote Sensing Signal and Image Processing Laboratory, University of Maryland Baltimore County, Baltimore; with the Applied Information Sciences Branch, Goddard Space Flight Center, Greenbelt, MD; and with the AVIRIS Data Facility, Jet Propulsion Laboratory, Pasadena, CA. He is currently an Associate Professor with the Department of Technology of Computers and Communications, University of Extremadura, Caceres, Spain, where he is the Head of the Hyperspectral Computing Laboratory. He is the author or coauthor of more than 260 publications on remotely sensed hyperspectral imaging, including more than 40 Journal Citation Report papers, 20 book chapters, more than 150 peer-reviewed conference proceeding papers, one book and several special issues guest edited in different journals. His research interests include remotely sensed hyperspectral imaging, pattern recognition, signal and image processing, and efficient implementation of large-scale scientific problems on parallel and distributed

computing architectures.

computer architectures. Dr. Plaza currently serves as Associate Editor for the IEEE Transactions on Geoscience and Remote Sensing journal, where he received the recognition of Best Reviewers in 2010. He is also a recipient of the recognition of Best Review-

ers of the IEEE Geoscience and Remote Sensing Letters journal in 2009.